# SPACE VLBI OBSERVATIONS OF 3C 279 AT 1.6 AND 5 GHZ

B. G. Piner[1], P. G. Edwards[2], A. E. Wehrle[1], H. Hirabayashi[2], J. E. J. Lovell[3], & S. C. Unwin[1]

## ABSTRACT

We present VLBI Space Observatory Programme (VSOP) observations of the gamma-ray blazar 3C 279 at 1.6 and 5 GHz made on 1998 January 9-10 with the HALCA satellite and ground arrays including the Very Long Baseline Array (VLBA). The combination of the VSOP and VLBA-only images at these two frequencies maps the jet structure on scales from 1 to 100 mas. On small angular scales the structure is dominated by the quasar core and the bright secondary component 'C4' located 3 milliarcseconds from the core (at this epoch) at a position angle of $-115°$. On larger angular scales the structure is dominated by a jet extending to the southwest, which at the largest scale seen in these images connects with the smallest scale structure seen in VLA images. We have exploited two of the main strengths of VSOP: the ability to obtain matched-resolution images to ground-based images at higher frequencies and the ability to measure high brightness temperatures. A spectral index map was made by combining the VSOP 1.6 GHz image with a matched-resolution VLBA-only image at 5 GHz from our VSOP observation on the following day. The spectral index map shows the core to have a highly inverted spectrum, with some areas having a spectral index approaching the limiting value for synchrotron self-absorbed radiation of $\alpha = +2.5$ (where $S \propto \nu^{+\alpha}$). Gaussian model fits to the VSOP visibilities revealed high brightness temperatures ($> 10^{12}$ K) that are difficult to measure with ground-only arrays. An extensive error analysis was performed on the brightness temperature measurements. Most components did not have measurable brightness temperature upper limits, but lower limits were measured as high as $5 \times 10^{12}$ K. This lower limit is significantly above both the nominal inverse Compton and equipartition brightness temperature limits. The derived Doppler factor, Lorentz factor, and angle to the line-of-sight in the case of the equipartition limit are at the upper end of the range of expected values for EGRET blazars.

*Subject headings:* quasars: individual (3C 279) — galaxies: active — galaxies: jets — techniques: interferometric — radio continuum: galaxies — radiation mechanisms: non-thermal

## 1. INTRODUCTION

The quasar 3C 279 ($z$=0.536) is one of the most intensively studied quasars for several reasons. It was the first radio source observed to exhibit superluminal motion (Knight et al. 1971; Whitney et al. 1971; Cohen et al. 1971). It was the first blazar — and remains one of the brightest — detected in high-energy $\gamma$-rays by the EGRET instrument on the *Compton Gamma Ray Observatory* (Hartman et al. 1992). The EGRET detection prompted several large multiwavelength studies of this source. Results of these studies are presented by Maraschi et al. (1994), Grandi et al. (1996), Hartman et al. (1996), and Wehrle et al. (1998). The radio flux density of 3C 279 has been monitored by the Michigan group since 1965 at frequencies of 4.8, 8.0, and 14.5 GHz (Aller et al. 1985). The observations presented in this paper occurred at the beginning of a total flux density flare that would later reach the highest flux densities yet recorded in this program for 3C 279. [4]

Following the discovery of superluminal motion, the parsec scale structure of 3C 279 has been monitored using the VLBI technique. Cotton et al. (1979) measured a speed of 15 $c$ for the original superluminal jet component. (Throughout the paper we assume $H_0$=70 km s$^{-1}$ Mpc$^{-1}$ and $q_0$=0.1, and component speeds measured by others have been expressed in these terms.) Unwin et al. (1989) and Carrara et al. (1993) describe VLBI monitoring of 3C 279 at 5, 11, and 22 GHz throughout the 1980s. These authors observed the motions of several new superluminal components, and found that the speeds of these components were only one-quarter to one-third (3-5 $c$) of that measured for the original superluminal component during the 1970s. VLBI monitoring of 3C 279 has been undertaken at 22 and 43 GHz during the 1990s. Initial results of this high-frequency monitoring are reported by Wehrle, Unwin, & Zook (1994) and Wehrle et al. (1996), and final results will be reported by Wehrle et al. (2000). High-resolution VLBI polarimetric images of 3C 279 have been made by Leppänen, Zensus, & Diamond (1995), Lister, Marscher, & Gear (1998) and Wardle et al. (1998). The detection of circularly polarized radio emission by Wardle et al. provides some of the first direct evidence that electron-positron pairs are an important component of the jet plasma. One notable feature of the VLBI observations of this source has been the differing speeds and position angles of the VLBI components. Carrara et al. (1993) and Abraham & Carrara (1998) claim that these can be explained by ejection of components by a precessing jet.

[1]Jet Propulsion Laboratory, California Institute of Technology, 4800 Oak Grove Dr., Pasadena, CA 91109; B.G.Piner@jpl.nasa.gov, Ann.E.Wehrle@jpl.nasa.gov, Stephen.C.Unwin@jpl.nasa.gov

[2]Institute of Space and Astronautical Science, Sagamihara, Kanagawa 229-8510, Japan; pge@vsop.isas.ac.jp, hirax@vsop.isas.ac.jp

[3]Australia Telescope National Facility, PO Box 76, Epping NSW 1710, Australia; Jim.Lovell@atnf.csiro.au

[4]http://www.astro.lsa.umich.edu/obs/radiotel/gif/1253-055.gif

3C 279 was observed during the TDRSS space VLBI experiments at 2.3 GHz (Linfield et al. 1989) and 15 GHz (Linfield et al. 1990), with source frame brightness temperatures between 1.6 and 2.0 $\times$ $10^{12}$ K being measured for this source. A brightness temperature of 1.9 $\times$ $10^{12}$ K (translated from observed frame to source frame) was also measured for 3C 279 in the 22 GHz VSOP Pre-Launch Survey (Moellenbrock et al. 1996). This source has been detected in VLBI observations up to frequencies of 215 GHz (Krichbaum et al. 1997). This paper reports on the VSOP observations of 3C 279 made during the first Announcement of Opportunity period (AO1). Hirabayashi et al. (1999) and Edwards et al. (1999) presented preliminary analyses of these 5 and 1.6 GHz VSOP observations respectively. Here we present higher dynamic range images together with analysis and interpretation of model fits and a spectral index map.

## 2. OBSERVATIONS

The quasar 3C 279 was observed on two consecutive days during the AO1 phase of the VSOP mission: on 1998 January 9 at 1.6 GHz, and on 1998 January 10 at 5 GHz. The VSOP mission uses the Japanese HALCA satellite as an element in a changeable VLBI array in order to obtain visibility measurements on baselines larger than the Earth's diameter. HALCA was launched on 1997 February 12 and carries an 8 meter antenna through an elliptical orbit with an apogee height of 21,400 km (yielding baselines up to 2.6 Earth diameters), a perigee height of 560 km, and an orbital period of 6.3 hours. HALCA has operational observing bands at 1.6 and 5 GHz (18 and 6 cm). The data from the satellite are recorded by a network of ground tracking stations and subsequently correlated with the data from the participating ground telescopes. The VSOP system and initial science results are discussed by Hirabayashi et al. (1998).

The observations of 1998 January 9–10 were conducted using the standard VSOP observing mode: two 16 MHz intermediate frequency bands, each 2-bit sampled at the Nyquist rate in left circular polarization, for a total data rate of 128 Mbps. The ground telescope arrays were made up of nine elements of the NRAO Very Long Baseline Array[5] (VLBA) — Hancock did not observe because of a power failure — with the addition of the 70 m telescopes at Goldstone, California, U.S.A. and Tidbinbilla, Australia on January 9, and the 64 m telescope at Usuda, Japan on January 10. The total observing time on January 9 was 6 hours, including 3.5 hours of HALCA data from the tracking station at Green Bank, West Virginia, covering the portion of HALCA's orbit from near perigee to near apogee. The data from Goldstone were not used in the final image as it observed for only a short time and there were significant calibration uncertainties with this data. The total observing time on January 10 was 10 hours, although for the final 1.5 hours only Mauna Kea, Usuda and HALCA observed and this data was also excluded from the final image (as four telescopes are required for amplitude self-calibration). This observation included two HALCA tracking passes of 3 hours each (separated by 4 hours) by the tracking stations at Robledo, Spain and Goldstone, California, U.S.A. Each tracking pass covered the portion of HALCA's orbit from near perigee to near apogee. The data from both observations were correlated at the VLBA correlator in Socorro. Through the remainder of this paper, we use "VSOP" to refer to the HALCA+ground-array combination.

Calibration and fringe-fitting were done with the AIPS software package. 3C 279 is a strong source, and good fringes were found to HALCA during all tracking passes. The antenna gain for Saint Croix had to be adjusted upward by a factor of $\sim$ 2 from its nominal value at 5 GHz since the VSOP observations were conducted at 4800–4832 MHz because HALCA's performance is better at these frequencies. Figure 1 shows the $(u, v)$ plane coverages of the two observations. These $(u, v)$ plane coverages result in highly elliptical beams: the major to minor axis ratio of the 5 GHz beam is 8:1. The addition of Tidbinbilla to the 1.6 GHz observation improves the north-south coverage and reduces this ratio to 4:1. Plots of correlated flux density vs. $(u, v)$ distance projected along a position angle of $-115°$ (the position angle of the brightest structure) are shown in Figure 2. The addition of HALCA extends the projected $(u, v)$ distances compared to the ground-only baselines from 120 to 340 M$\lambda$ at 5 GHz, and from 65 to 120 M$\lambda$ at 1.6 GHz. The beating evident in the correlated flux densities indicates that on milliarcsecond scales the morphology is dominated by two components of similar flux density.

## 3. RESULTS

### 3.1. *Images*

Images from these datasets were produced using standard CLEAN and self-calibration procedures from the Difmap software package (Shepherd, Pearson, & Taylor 1994). Figure 3 shows two images from the 5 GHz observation on 1998 January 10: the full-resolution space VLBI image and the VLBA-only image made from the same dataset with the space baselines removed. Figure 4 shows the full-resolution space VLBI and the VLBA-only images from the 1.6 GHz observation on the previous day (Tidbinbilla baselines were also removed from this ground-only image to reduce the size of the $(u, v)$ holes). The VSOP images are displayed using uniform weighting (although cleaning was done with both uniform and natural weighting to model the extended structure), while the VLBA images are displayed with natural weighting. We stress the importance of using uniform weighting with VSOP datasets. A naturally weighted VSOP image degrades the resolution of the ground-space array because of the higher weighting of the larger ground antennas and the much denser sampling of the $(u, v)$ plane on the ground baselines.

The VSOP and VLBA-only images differ in scale by about a factor of four, showing the greatly increased resolution provided by the space baselines. The VSOP images presented in Figures 3 and 4 are the highest resolution images yet produced of 3C 279 at these frequencies. The 1.6 and 5 GHz VSOP images have formal dynamic ranges (peak:rms) of 1,500:1 and 2,000:1 respectively, demonstrating that high dynamic range images can be made de-

[5]The National Radio Astronomy Observatory is a facility of the National Science Foundation operated under cooperative agreement by Associated Universities, Inc.

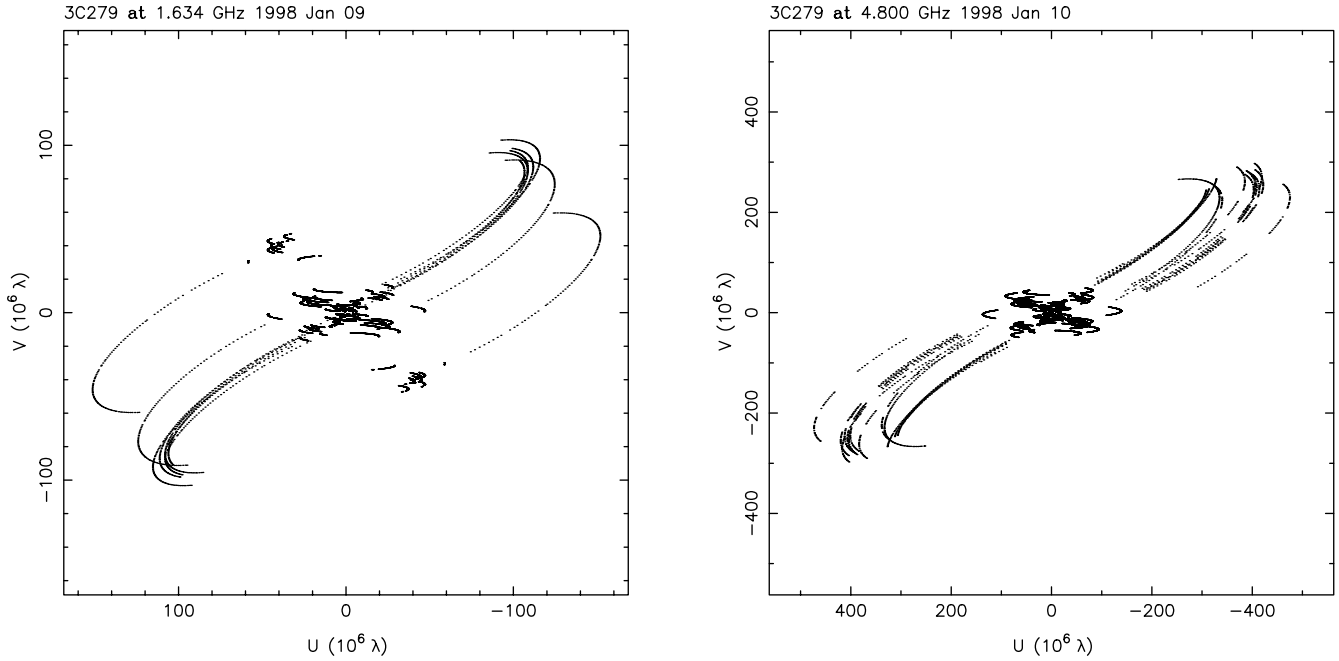


FIG. 1.— $(u, v)$ plane coverages for the VSOP observations of 3C 279. The left panel shows the 1.6 GHz coverage, the right panel the 5 GHz coverage.

spite the small size of the HALCA orbiting antenna. For comparison, the VLBA-only images have dynamic ranges of 5,000:1 and 15,000:1 respectively. The 5 GHz VSOP image shows that on small angular scales 3C 279 is dominated by a double structure. This structure consists of the compact core and inner jet region (the feature to the east) and a bright jet component about 3 mas from the core along a position angle of $-115°$ (the feature to the west). This bright jet component, 'C4', is a well known feature first observed in 1985. This component will be discussed further in § 4.1.

The structure on slightly larger angular scales is quite different. The 5 GHz VLBA image and the 1.6 GHz VSOP image both show the double structure mentioned above (although in the 1.6 GHz image the jet component is brighter than the core which results in the jet component being placed at the phase center), as well as a more extended jet to the southwest along a position angle of approximately $-140°$. This position angle is similar to that seen in older VLBI images (see § 4.1) as well as VLA and MERLIN images (de Pater & Perley 1983; Pilbratt, Booth, & Porcas 1987; Akujor et al. 1994). The resolutions of the 5 GHz VLBA image and the 1.6 GHz VSOP image are roughly equal, a fact that allows a spectral index map to be made from these images (§ 4.2). The jet emission in the 1.6 GHz VSOP image is quite complex, and it appears in Figure 4 that the jet may be limb brightened. However, we caution against over-interpreting these complex jet features because the CLEAN striping produced by the holes in the $(u, v)$ plane coverage runs parallel to the jet, and because simulations indicate that, due to the lack of complete $(u, v)$ plane coverage, space VLBI images may show such knotty structure when the actual brightness distribution is smoother (D. Murphy 1999, private communication). The 1.6 GHz VLBA image shows structure extending out to $\sim 100$ mas from the core, all the way out to the smallest size scales sampled by the 22 GHz VLA images of de Pater & Perley (1983).

### 3.2. *Model Fits*

The Difmap model-fitting routine was used to fit elliptical Gaussian components to the visibility data for each image in Figures 3 and 4. When model fitting VSOP data, it is important to increase the weight of HALCA over the default weighting used by Difmap in order for the space baseline data to have any effect on the model. We increased the weight of HALCA during model fitting by a factor equal to the product of the ratios of the average ground baseline sensitivity to the average space baseline sensitivity ($\sim 50$ for these observations) and the number of ground visibilities to the number of space visibilities ($\sim 10$ for these observations). This effectively achieves a "uniform" weighting during model fitting, and causes the space visibilities to have an effect on the model fitting equal to that of the ground visibilities.

The results of the model fitting are given in Table 1. Component numbers are given only for ease of later reference, and are not meant to identify the same component between images. Tentative component identifications obtained from the discussion in § 4.1 are given in the third column. Note that the lower resolution images (e.g. the 1.6 GHz VLBA image) may not properly split the flux between the core and the closest component. In each case we have taken the far northeastern component to be the core, and have defined the other component positions relative to the position of the core. In the 1.6 GHz VSOP image, the southwestern jet is too complex to be fit with simple Gaussian components, and we left the CLEAN components in this region during model fitting. When fitting elliptical components, the model fitting chi-squared statis-

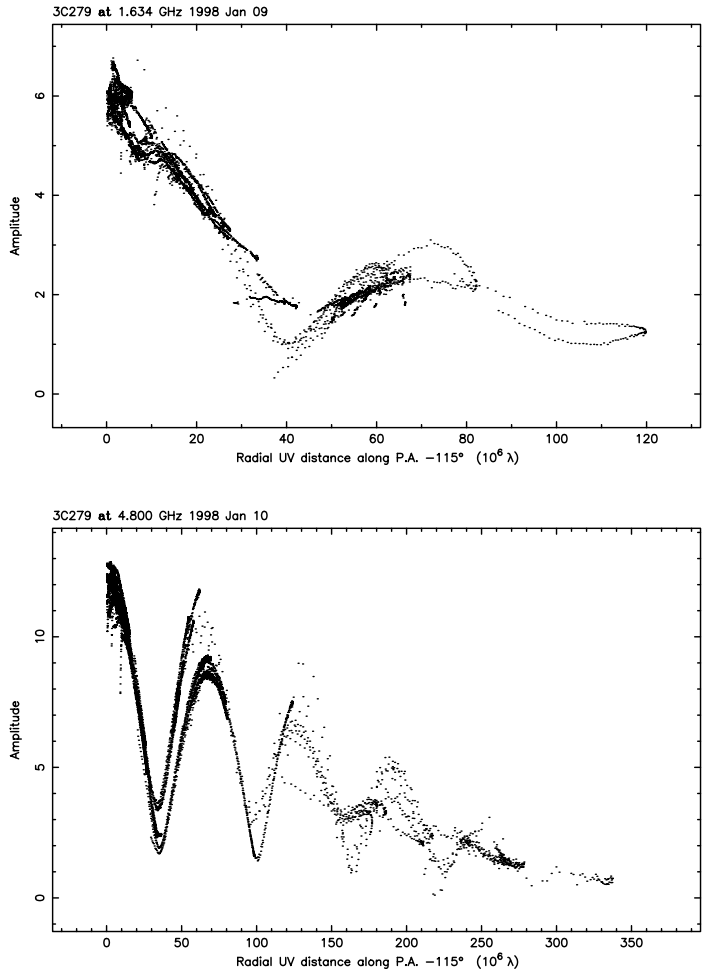


FIG. 2.— Correlated flux density in Janskys vs. projected $(u, v)$ distance along position angle $-115°$. The top panel shows the 1.6 GHz observation, the bottom the 5 GHz observation.

tic is frequently minimized by an ellipse of zero axial ratio. This is unphysical in the sense that these components have formally infinite brightness temperatures. In these cases an upper limit to the size of the component can be used instead of the best-fit value to find a lower limit to the brightness temperature. Since we use an error analysis method to find these limits in § 4.3, we have left these zero axial ratio components in the models if they minimize the chi-squared for that model. Table 1 also gives the source frame brightness temperatures for the VSOP models, where the maximum brightness temperature of a Gaussian component is given by

$$T_B = 1.22 \times 10^{12} \, \frac{S(1+z)}{ab\nu^2} \, \mathrm{K}, \qquad (1)$$

where $S$ is the flux density of the component in Janskys, $a$ and $b$ are the FWHMs of the major and minor axes respectively in mas, $\nu$ is the observation frequency in GHz, and $z$ is the redshift.

## 4. DISCUSSION

### 4.1. *Identification of Historical Components*

In this section we consider the identification of components seen in these images with previously published VLBI components, using these components' published positions and velocities. We work from the innermost components outward, starting with the components fit to the 5 GHz VSOP image. We caution that any such identifications are highly speculative, particularly for the older components where much time has elapsed since the last published image. Note that prior to completion of the NRAO VLBA (1995), global VLBI network sessions at 22 GHz occurred only twice per year and used less than half a dozen antennas.

A total of six elliptical Gaussian components are required to fit the 5 GHz VSOP data. The first three of these components are interior to 1 mas, and represent the core and two components of the inner jet. The region interior to 1 mas has been studied by Wehrle et al. (2000) at 22 and 43 GHz and Rantakyrö et al. (1998) at 86 GHz, and they find it to be a complex region with multiple components. Attempts to name components in this region have resulted in some confusion. The component named 'C5' in three 11 GHz maps from 1989.3-1991.1 by Carrara et al. (1993) and Abraham & Carrara (1998) is not the same component referred to as either 'C5' by Wehrle et al. (1994) at 22 GHz, Leppänen et al. (1995) at 22 GHz, and Lister et al. (1998) at 43 GHz or 'the stationary 1 mas feature' by Wehrle et al. (1996) at 22 GHz. Wehrle et al. (1994) and

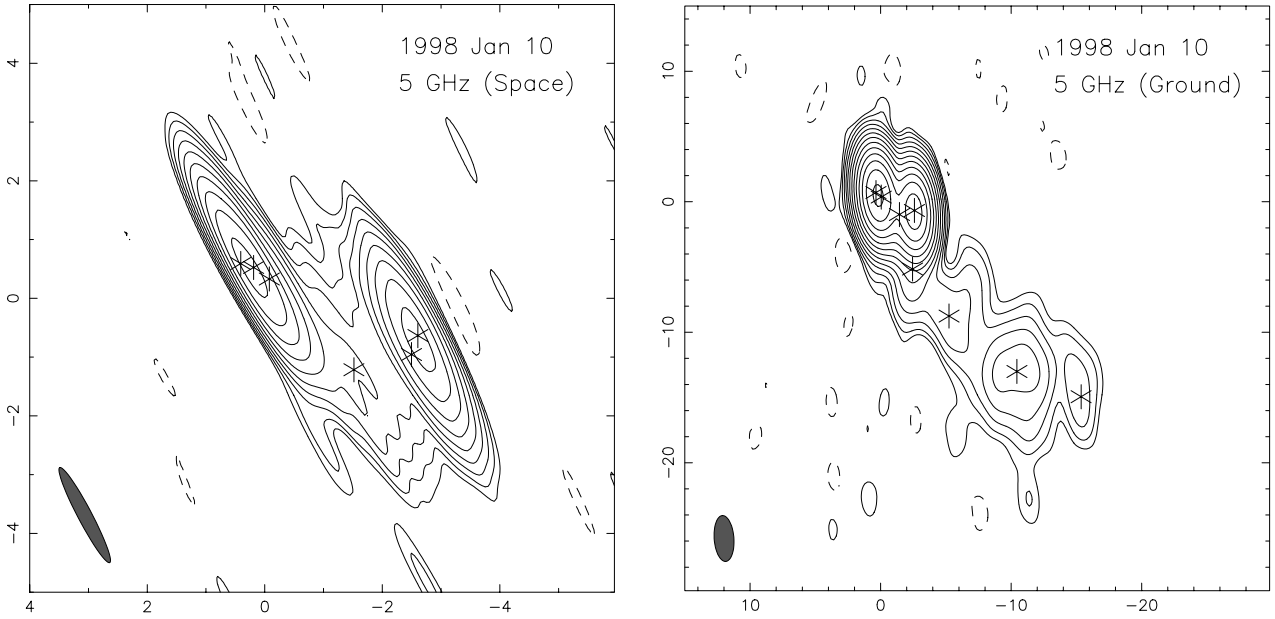


FIG. 3.— Images of 3C 279 from the 5 GHz VSOP observation on 1998 January 10. The image on the left is the full-resolution space VLBI image, the image on the right is the VLBA-only image made from the same dataset with the space baselines removed. The lowest contour in each image has been set equal to 3 times the rms noise level in that image. The peak flux densities are 3.98 and 6.67 Jy beam$^{-1}$, the contour levels are 6.0 mJy beam$^{-1}$ × 1,2,4,...512 and 1.4 mJy beam$^{-1}$ × 1,2,4,...4096, and the beam sizes are 1.83 × 0.24 mas at 28° and 3.52 × 1.51 mas at 4° for the space and ground images respectively. Model-fit component positions are marked with asterisks.

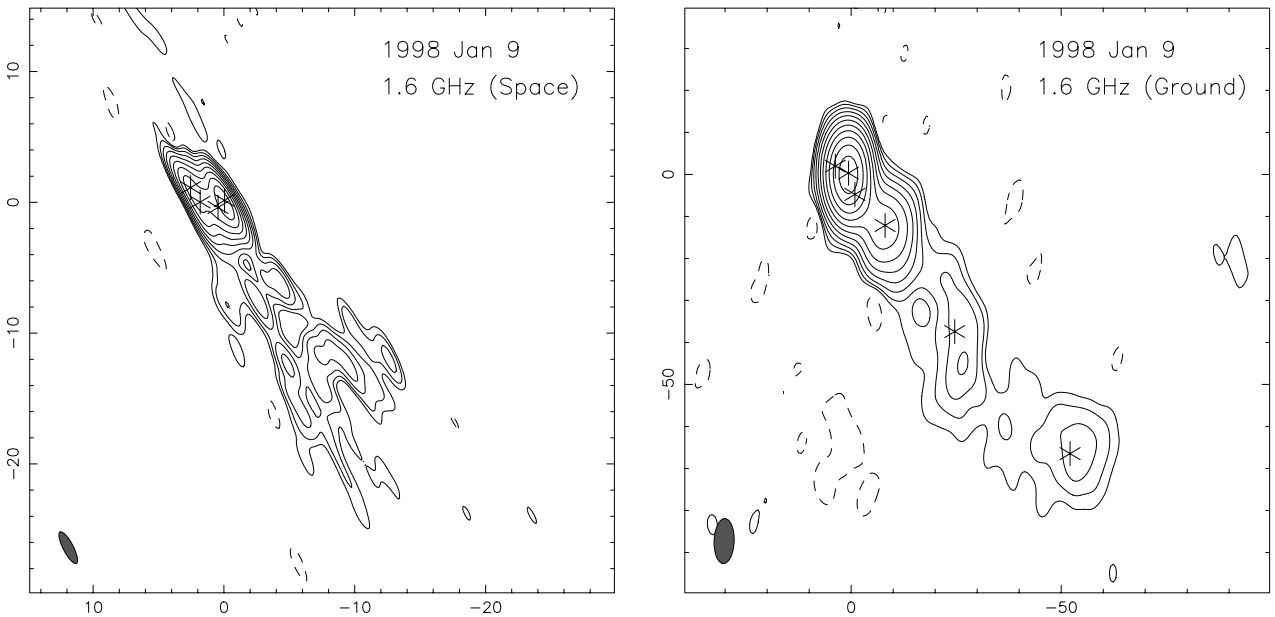


FIG. 4.— Images of 3C 279 from the 1.6 GHz VSOP observation on 1998 January 9. The image on the left is the full-resolution space VLBI image, the image on the right is the VLBA-only image made from the same dataset with the space and Tidbinbilla baselines removed. The lowest contour in each image has been set equal to 3 times the rms noise level in that image. The peak flux densities are 2.29 and 4.73 Jy beam$^{-1}$, the contour levels are 4.7 mJy beam$^{-1}$ × 1,2,4,...256 and 2.9 mJy beam$^{-1}$ × 1,2,4,...1024, and the beam sizes are 2.71 × 0.77 mas at 28° and 10.7 × 4.77 mas at −2° for the space and ground images respectively. Model-fit component positions are marked with asterisks.

Wehrle et al. (1996) identify a component between C5 and the core, and Leppänen et al. (1995) identify two components in this region which they name 'C6' and 'C7'. Lister et al. (1998) do not detect these components but record another new component named 'C8'. Clarification of the components in this region must await completion of the Wehrle et al. (2000) analysis.

The situation beyond ∼ 1 mas is easier to interpret. The bright feature at ∼ 3 mas is the component C4 that has been seen by many other authors (Unwin et al. 1989; Carrara et al. 1993; Wehrle et al. 1994; Leppänen et al. 1995; Wehrle et al. 1996; Lister et al. 1998; Wardle et al. 1998; Kellermann et al. 1998). This component has been moving along a position angle of −115° for over 10 years. The brightness distribution of C4 is asymmetric, with the leading edge being sharper than the trailing edge, and two

Table 1
Gaussian Models

| Image | Comp. # | Tentative[a] ID | $S$[b] (Jy) | $r$[c] (mas) | PA[c] (deg) | $a$[d] (mas) | $b/a$ | $\Phi$[e] (deg) | $T_B$[f] ($10^{12}$ K) |
|---|---|---|---|---|---|---|---|---|---|
| 5 GHz VSOP | 1 | Core | 1.71 | 0.00 | ... | 0.28 | 0.00 | 29.8 | ... |
| | 2 | | 3.91 | 0.23 | –107.1 | 0.56 | 0.35 | 38.6 | 2.90 |
| | 3 | | 1.36 | 0.55 | –118.4 | 0.83 | 0.35 | 44.4 | 0.46 |
| | 4 | C3? | 0.83 | 2.64 | –133.2 | 2.53 | 0.52 | 36.4 | 0.02 |
| | 5 | C4 | 3.39 | 3.26 | –112.1 | 0.46 | 0.50 | –12.7 | 2.63 |
| | 6 | C4 | 0.79 | 3.29 | –118.1 | 0.97 | 0.25 | 34.3 | 0.28 |
| 5 GHz VLBA | 1 | Core | 4.17 | 0.00 | ... | 0.29 | 0.00 | 41.5 | |
| | 2 | | 2.87 | 0.53 | –130.9 | 0.38 | 0.00 | –81.7 | |
| | 3 | C3? | 0.64 | 2.47 | –133.1 | 1.50 | 0.71 | 2.0 | |
| | 4 | C4 | 4.23 | 3.25 | –115.0 | 0.63 | 0.51 | –2.3 | |
| | 5 | C2? | 0.06 | 6.50 | –154.4 | 2.78 | 0.33 | –12.1 | |
| | 6 | C2? | 0.05 | 11.00 | –149.4 | 3.47 | 0.56 | 34.0 | |
| | 7 | C1? | 0.14 | 17.45 | –141.8 | 4.58 | 0.85 | –7.1 | |
| | 8 | | 0.01 | 22.18 | –134.9 | 3.15 | 0.29 | 6.4 | |
| 1.6 GHz VSOP [g] | 1 | Core | 0.76 | 0.00 | ... | 1.95 | 0.00 | 34.4 | ... |
| | 2 | | 0.92 | 1.33 | –146.4 | 2.29 | 0.35 | 20.5 | 0.35 |
| | 3 | C3? | 1.57 | 2.59 | –125.9 | 1.93 | 0.16 | 55.4 | 1.92 |
| | 4 | C4 | 2.21 | 2.77 | –110.6 | 0.95 | 0.00 | 43.1 | ... |
| 1.6 GHz VLBA | 1 | Core | 0.23 | 0.00 | ... | 10.64 | 0.00 | 5.9 | |
| | 2 | C4 | 5.09 | 3.55 | –117.9 | 2.71 | 0.51 | 55.8 | |
| | 3 | C2? | 0.35 | 8.20 | –145.3 | 7.69 | 0.00 | 25.0 | |
| | 4 | C1? | 0.61 | 18.45 | –140.0 | 7.44 | 0.45 | 64.6 | |
| | 5 | | 0.13 | 48.58 | –144.2 | 27.19 | 0.46 | 33.2 | |
| | 6 | 'C' | 0.14 | 88.35 | –140.8 | 60.26 | 0.28 | 65.1 | |

[a] Tentative component identifications from the discussion in § 4.1. A question mark indicates a more speculative identification.
[b] Flux density in Janskys. Note that the lower resolution images (e.g. the 1.6 GHz VLBA image) may not properly split the flux between the core and the closest component.
[c] $r$ and PA are the polar coordinates of the center of the component relative to the presumed core. Position angle is measured from north through east.
[d] $a$ and $b$ are the FWHM of the major and minor axes of the Gaussian component.
[e] Position angle of the major axis measured from north through east.
[f] Maximum source frame Gaussian brightness temperatures are given for the VSOP models.
[g] The southwestern jet is fit by clean components in this model.

model components are required to represent it (components 5 and 6 in the 5 GHz VSOP model). The 43 GHz data of Wehrle et al. (2000) also require two components to represent the structure of C4. The sharp leading edge of this component is suggestive of a working surface or shock front. The polarization observations of Leppänen et al. (1995), Lister et al. (1998), and Wardle et al. (1998) show that C4 has a magnetic field transverse to the jet, also indicative of a shock front. Carrara et al. (1993) determined a motion of 0.15±0.01 mas/yr (4 $c$) for C4, however the position of C4 in our 5 GHz image is inconsistent with a simple extrapolation at this speed. However, we note that at the time of the observations of Carrara et al. C4 was ∼1 mas from the core and in the region noted above as being difficult to interpret. More recent data from Wehrle et al. (2000) and Kellermann (1999, private communication) indicate a speed of ∼7 $c$ for C4 between 1991 and 1999, which is consistent with the position seen in the VSOP images in this paper. Although the larger scale structure has a much different position angle than C4, C4 shows no signs of altering its path to follow the larger scale structure, and appears to be continuing along a position angle of −115°. Component C4 dominates the emission in the 1.6 GHz VSOP image and it is represented by component 4 in the 1.6 GHz VSOP model.

Older VLBI measurements (Cotton et al. 1979; Unwin et al. 1989; Carrara et al. 1993) followed a series of components (C1–C3) moving along position angles of −130 to −140°. Since this is also the position angle of the larger scale structure seen in our images, it is reasonable that this string of components may form the southwestern jet in our images. The 5 GHz VSOP image shows a fainter, more diffuse component at a position angle of −133° located ∼2.6 mas from the core (component 4 in the 5 GHz model, component 3 in the 1.6 GHz model). Emission is also seen at this position in the images of Kellermann et al. (1998) and Wehrle et al. (2000). An attempt to identify this component with the most recent component ejected along this position angle (C3) would imply a drastic deceleration for C3; a straightforward extrapolation of the

motion of C3 given by Carrara et al. (1993) would place it at a separation of 4 mas in 1998 and so we consider such an identification unlikely. An extrapolation of the motion of C2 estimated from the positions given by Unwin et al. (1989) would place C2 between 6 and 10 mas from the core at the epoch of our VSOP observations, and conceivably identify it with either component 5 or 6 in the 5 GHz VLBA model (component 3 in the 1.6 GHz VLBA model). Cotton et al. (1979) reported a large proper motion of 0.5 mas/yr during the early 1970s; their data was re-examined and their interpretation judged to be correct by Unwin et al. (1989). An extrapolation the motion of the Cotton et al. (1979) component (which could also be the component C1 of Unwin et al. [1989] located ∼8 mas from the core at 1984.25) would place it about 15 mas from the core in 1998, and mean that it could be identified with the relatively bright component 7 of the 5 GHz VLBA model (component 4 in the 1.6 GHz VLBA model). The uncertainties of extrapolating component motions makes this analysis highly speculative; the validity of the assumption of constant projected speed with time is unclear, and enough time has elapsed that the fate of these older components will probably never be certain.

A series of VLA maps of 3C 279 at varying resolution has been published by de Pater & Perley (1983). Their highest resolution map shows a component (component 'C') 95 mas from the core in position angle −145°. (This map has a higher resolution than the MERLIN maps of Pilbratt et al. [1987] and Akujor et al. [1994] because it is at a higher frequency). Our 1.6 GHz VLBA image extends out to this distance from the core, and we see a 140 mJy component at 88 mas in position angle −141° (component 6 in the 1.6 GHz VLBA model). We can tentatively identify this with component C of de Pater & Perley (1983), given the large errors implied by their VLA beam (60 mas resolution) and the similar size of our model-fit component. These errors make it impossible to infer anything about the motion of this component between 1982 and 1998. We have, however, matched the largest scale VLBI structures with the smallest scale VLA structures, and established a continuous connection between the parsec and kiloparsec scales in this source.

### 4.2. *Spectral Index Map*

Construction of spectral index maps is often hindered by the differing resolutions of the images at different frequencies; however, a unique capability of the VSOP mission is that it can provide matched resolution images to ground-based images at higher frequencies, enabling the construction of a spectral index map from two images of approximately equal resolution. We have used this capability to produce a spectral index map from the 1.6 GHz VSOP image and the 5 GHz VLBA-only image; this spectral index map is shown in Figure 5. These two datasets were taken only 1 day apart, so the errors due to component motions are negligible. To produce the spectral index map the two images were restored with their average beam of 3.12 × 1.14 mas with a major axis position angle of 15.9°, each image was restored from the clean components without residuals (the flux left over after the clean components convolved by the dirty beam have been subtracted from the data), and no spectral index was calculated for pixels where the flux densities were less than 3 times the rms noise level in the images at both frequencies. (A spectral index map using images restored from clean components *with* residuals was also produced and gave essentially the same results. We prefer to use the images without residuals as the residuals can then be used to assess the possible errors in the spectral index map.) In the following discussion we use $S \propto \nu^{+\alpha}$.

A major difficulty in making spectral index maps lies in correctly registering the two images. We investigated several alignments of these two images, including aligning the peak core pixels and aligning the peak pixels in the bright jet component (C4). We doubled the number of pixels across each image in order to measure the required shifts as accurately as possible. Aligning the peak core pixels produced unphysical results, including a highly inverted spectral index along the right edge of component C4. Of the different alignments tried, aligning the peak pixels in the jet component C4 produced the most physically reasonable results. The reason for this can be seen *a posteriori* from Figure 5. The spectral index is constant across component C4, meaning that the brightest pixels in C4 at 1.6 and 5 GHz will represent the same physical location. On the other hand, there are steep spectral index gradients across the core region, so the peak pixel in the core region will be at different locations at 1.6 and 5 GHz.

We also constructed a map of the error in the spectral index; this error map is shown in Figure 6. The error was calculated by standard propagation of errors, using the fluxes at each pixel in each residual map as the flux errors. This method actually gives a lower limit to the error at each pixel, because it does not take into account calibration errors or errors in imaging the source structure caused by the holes in the $(u, v)$ plane coverage. In the region comprising the southwestern jet the errors in the spectral index $\alpha$ range from ±0.05 in the brighter parts of the jet (the knot at ∼ 18 mas) to ±0.3 in the fainter parts. The formal errors in the core and C4 regions are quite low and so the errors in these regions will be dominated by the other effects mentioned above.

The core of 3C 279 has an inverted spectrum with steep spectral index gradients. Such inverted spectra are commonly interpreted as being due to self-absorption of the radio synchrotron emission. The calculated spectral index in the core region ranges from ∼ 1.0 at the western edge to the theoretical limiting value for synchrotron self-absorption of 2.5 (assuming a constant magnetic field) over a small region at the eastern edge. Spectral indices approaching this theoretical value are almost never seen; the flatter spectra usually observed are commonly interpreted as being due to an inhomogeneous source made up of a number of synchrotron components with differing turnover frequencies (e.g. Cotton et al. 1980). The highly inverted spectrum at the eastern edge may imply the detection of a homogeneous compact component in this region, which should be an efficient producer of inverse Compton gamma-rays. The spectral index gradients in the core imply that components will have different measured separations at different frequencies. We do indeed observe this frequency-dependent separation, the measured separation between the core and C4 model components is 3.3 mas at 5 GHz and only 2.8 mas at 1.6 GHz. The fact that the apparent position of the core is a function of wavelength is an important verification of the twin

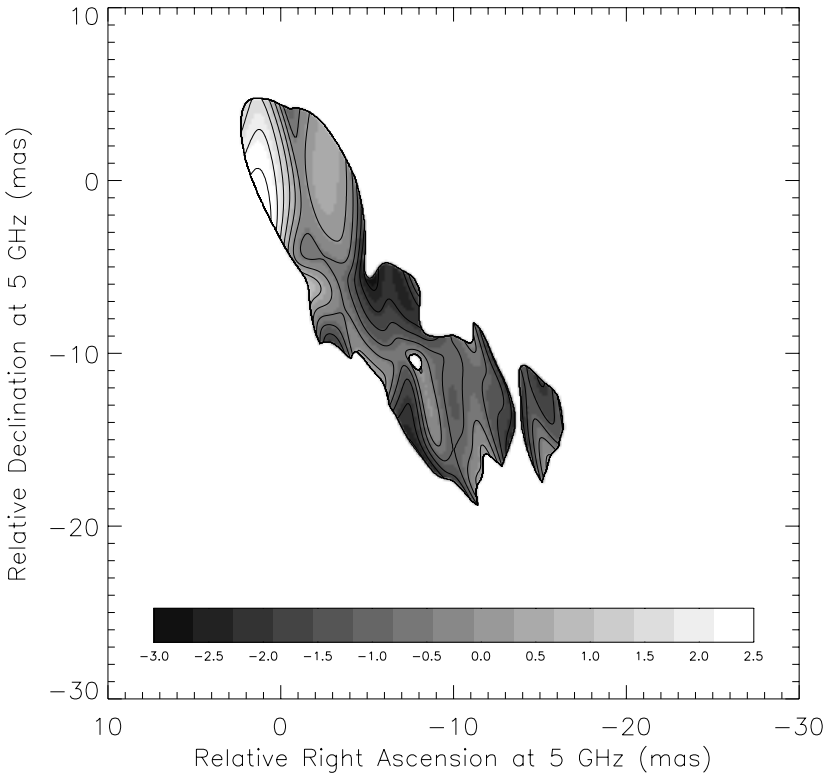


FIG. 5.— Spectral index map of 3C 279 made from the 1.6 GHz VSOP image and the 5 GHz VLBA image. The gray-scale color bar along the bottom of the image indicates the value of the spectral index ($S \propto \nu^{+\alpha}$), with lighter colors indicating an inverted spectrum and darker colors a steep spectrum. Spectral index contours are also plotted at intervals of 0.5, from −2.5 to 2.5. The beam used was the average of the 1.6 GHz VSOP beam and the 5 GHz VLBA beam, or 3.12 × 1.14 mas at 15.9°. The white pixels near the center of the jet represent an area where the flux was below the clipping level applied for calculation of the spectral index.

exhaust model, which argues that the observed core is that position in the throat of a nozzle where the opacity is of the order of unity.

The jet component C4 has a flat spectrum with $\alpha$ approximately 0.25. This is unusual, as jet components usually have steeper spectra ($\alpha < 0$). The southwestern jet also has structure in its spectral index distribution, with the edges of the jet appearing to have a steeper spectrum than the center. This spectral index structure is related to the apparent limb brightening at 1.6 GHz which, as noted above, should be interpreted with care. AO2 VSOP observations of 3C 279 at 1.6 GHz in which the baselines to the orbiting antenna have a different orientation in the $(u, v)$ plane will allow a consistency check on the brightness and spectral index structures transverse to the jet.

### 4.3. *High Brightness Temperatures*

Space VLBI observations have a major advantage over ground-based observations because they are able to measure higher brightness temperatures. This is because the smallest measurable major and minor axes in equation [1] are proportional to the resolution of the interferometer, which is proportional to 1/(baseline × frequency), so the denominator in equation [1] depends only on baseline length. The brightness temperature limit for ground-based VLBI is $\sim 10^{11} S(1+z)/f^2$ and that for space VLBI with HALCA is $\sim 10^{12} S(1+z)/f^2$, where $S$ is the flux density in Janskys, $z$ is the redshift, and $f$ is the smallest size that can be measured expressed as a percentage of the beam size. The improvement gained by space VLBI thus covers the interesting transition region around $10^{12}$ K, the nominal inverse Compton brightness temperature limit (Kellermann & Pauliny-Toth 1969).

Observed brightness temperatures are often used to calculate Doppler beaming factors by assuming an intrinsic brightness temperature and using the fact that $T_{B,obs} = \delta T_{B,int}$, where $T_{B,obs}$ is the observed source frame brightness temperature, $T_{B,int}$ is the intrinsic brightness temperature, and $\delta$ is the Doppler factor. The intrinsic brightness temperature depends on the physical mechanism imposing the limitation. Kellermann & Pauliny-Toth (1969) showed that inverse Compton losses limit the intrinsic brightness temperatures to $\sim 5 \times 10^{11} - 1 \times 10^{12}$ K, otherwise the source can radiate away most of its energy on a timescale of days. Readhead (1994) proposed that the limiting mechanism is equipartition of energy between the particles and magnetic field, and that intrinsic brightness temperatures are limited to $\sim 5 \times 10^{10} - 1 \times 10^{11}$ K.

To be complete, brightness temperature measurements must be presented with associated errors. Since the brightness temperature depends on the product of the major and minor axes of the model-fit component, and these axis sizes can have large errors, the measured brightness temperature can also have large errors. Error analysis of VLBI model-fit parameters has historically been problematic. In this paper we use the "Difwrap" program[6] (Lovell 2000) to

[6]http://halca.vsop.isas.ac.jp./survey/difwrap/

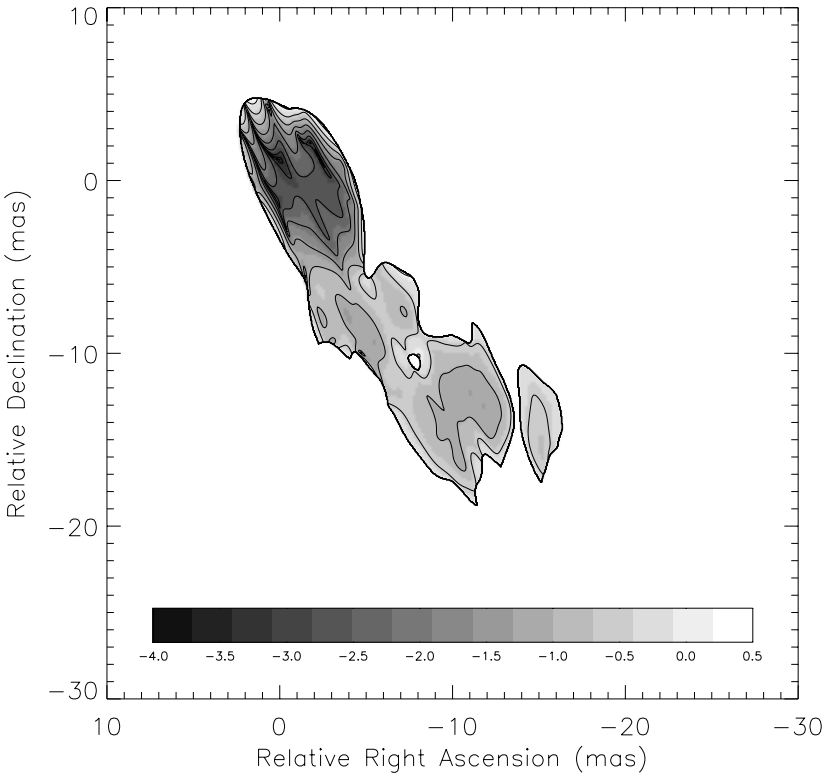


FIG. 6.— Error map for the spectral index map presented in Figure 5. The error was calculated by standard propagation of errors, using the fluxes at each pixel in each residual map as the flux errors. The gray-scale color bar along the bottom of the image indicates the value of the logarithm of the error in the spectral index, with lighter colors indicating a larger error. Contours of the logarithm of the error are plotted at intervals of 0.5, from −3.0 to 0.0.

analyze the upper and lower limits on our brightness temperature measurements. This program uses the method described by Tzioumis et al. (1989) in which the parameter of interest is varied in steps around the best-fit value, allowing the other parameters to relax at each step, and the resultant model is then visually compared with the data to determine whether or not the fit remains acceptable. The brightness temperature of a component depends on the flux density and size of the component, and the size depends on three of the Difmap model-fit parameters: the major axis length, the axial ratio, and indirectly on the position angle of the major axis (since different major axis lengths and axial ratios may be allowed at different position angles). The size error analysis therefore searches a three-dimensional cube in parameter space, varying the major axis length and position angle and the axial ratio over all possible combinations given input search ranges and step sizes. A visual inspection is done to determine the goodness of the fit instead of using a numerical cutoff in the chi-squared because the true number of degrees of freedom is not well known. Using the actual number of measured visibilities ($\sim 10^5$ for these observations) to determine the degrees of freedom gives errors that are unrealistically small, and methods used by other authors did not have a clear physical motivation (e.g. one degree of freedom per antenna per hour [Biretta, Moore, & Cohen 1986]).

In Table 2 we show our brightness temperature error analysis for the six components in Table 1 that have best-fit brightness temperatures over $10^{12}$ K. For each of these components we searched a $7 \times 7 \times 7$ cube in major axis length, axial ratio, and major axis position angle. Initially we searched major axis lengths from zero to twice the best-fit length, axial ratios from zero to one, and a range of $\pm 90°$ in position angle; and then refined the search to a smaller grid if necessary. The parameter values yielding the maximum and minimum area that still gave an acceptable fit to the data were recorded. A similar error analysis was done for the flux density, and the extreme allowed values of area and flux density were used to determine the maximum and minimum brightness temperatures. Since errors in flux density and size are searched for separately, the flux density was held constant during the size error analysis and vice-versa. The position of the component was also held constant to avoid it 'trading identities' with another model component. All other model components were allowed to vary.

Inspection of Table 2 shows that in all but one of the cases investigated the component shrinking to zero area and infinite brightness temperature (in all cases caused by a valid fit with zero axial ratio at some position angle) produced acceptable results, and therefore it appears that many measured brightness temperatures, even those measured by space VLBI, may have error bars that extend to infinity in the positive direction. The measured lower limits also indicate a considerable error in the best-fit brightness temperature values: three of the six components with best-fit brightness temperatures over $10^{12}$ K have minimum brightness temperatures under this value. The other three components have minimum brightness temperatures

TABLE 2
BRIGHTNESS TEMPERATURE LIMITS FOR COMPONENTS WITH BEST-FIT BRIGHTNESS TEMPERATURES $> 10^{12}$ K

| Freq. (GHz) | Comp.[a] | Flux (Jy) | Min. Flux (Jy) | Max.[b] Flux (Jy) | Area (mas$^2$) | Min. Area (mas$^2$) | Max. Area (mas$^2$) | $T_B$ ($10^{12}$ K) | Min. $T_B$ ($10^{12}$ K) | Max. $T_B$ ($10^{12}$ K) |
|---|---|---|---|---|---|---|---|---|---|---|
| 4.8 | 1 | 1.71 | 1.61 | ... | 0.0 | 0.0 | 0.114 | ... | 1.15 | ... |
| | 2 | 3.91 | 3.61 | ... | 0.110 | 0.0 | 0.146 | 2.90 | 2.01 | ... |
| | 5 | 3.39 | 3.06 | 3.60 | 0.105 | 0.070 | 0.274 | 2.63 | 0.91 | 4.19 |
| 1.6 | 1 | 0.76 | 0.63 | ... | 0.0 | 0.0 | 0.636 | ... | 0.70 | ... |
| | 3 | 1.57 | 1.05 | ... | 0.578 | 0.0 | 2.905 | 1.92 | 0.25 | ... |
| | 4 | 2.21 | 2.09 | ... | 0.0 | 0.0 | 0.299 | ... | 4.91 | ... |

[a]Component numbers from the VSOP model fits in Table 1.
[b]Upper limits to the component flux were not calculated for cases where the component had a minimum area of zero.

over $10^{12}$ K, with minimum brightness temperatures of 1.2, 2.0, and $4.9 \times 10^{12}$ K being measured for components 1 and 2 of the 5 GHz VSOP model fit (the core and first jet component) and component 4 of the 1.6 GHz VSOP model fit (C4) respectively. Bower & Backer (1998) and Shen et al. (1999) report brightness temperatures of $\sim 3 \times 10^{12}$ K from VSOP observations of NRAO 530 and PKS 1921−293 respectively, but without accompanying error analyses.

If a brightness distribution other than a Gaussian is used in the model fitting, the derived values of the brightness temperature will be different. For example, the brightness temperature of a homogeneous optically thick component is given by

$$T_B = 1.77 \times 10^{12} \, \frac{S(1+z)}{ab\nu^2} \text{ K},$$

where the constant in front is different from that in equation (1), and $a$ and $b$ are the lengths of the major and minor axes respectively rather than the FWHMs. The visibility of a homogeneous optically thick component drops to 50% at the same baseline length as a Gaussian when its diameter equals 1.6 times the Gaussian's FWHM (Pearson 1995), so we expect the homogeneous optically thick brightness temperature to be about 0.6 of the Gaussian brightness temperature (see also Hirabayashi et al. 1998 and in particular the correction in the erratum to this paper). We have fit homogeneous optically thick components to the data, and for the two components in Table 2 where neither component type goes to zero size (components 2 and 5 of the 5 GHz model fit) we measure brightness temperatures of 1.9 and $1.5 \times 10^{12}$ K respectively for homogeneous optically thick components rather than 2.9 and $2.6 \times 10^{12}$ K for Gaussian components, so we see about the expected decrease. Since the true brightness distribution is not known, and Gaussian components are the standard for VLBI model fitting and provide a somewhat better fit for these observations, we remained with Gaussian components.

Our highest brightness temperature lower limit of $\sim 5 \times 10^{12}$ K for component C4 at 1.6 GHz implies Doppler factor lower limits of 5 and 50 for the inverse Compton and equipartition brightness temperature limits respectively. A Doppler factor of 50 is at the upper end of the Doppler factor distributions expected for flux-limited samples of flat-spectrum radio sources (Lister & Marscher 1997) and gamma-ray sources (Lister 1998). Bower & Backer (1998) found similar values for the Doppler factor of NRAO 530 under these same two limiting conditions. If VSOP observations reveal a brightness temperature much higher than $5 \times 10^{12}$ K, or many brightness temperatures around $5 \times 10^{12}$ K, it may be difficult to reconcile the high Doppler factors implied by the equipartition brightness temperature limit with beaming statistics and with the relatively slow speeds measured in studies of apparent velocity distributions (e.g. Vermeulen 1995).

Using an estimated speed for C4 of 7 $c$ (see § 4.1), and assuming the pattern speed observed with VLBI equals the bulk fluid speed in the jet, bulk Lorentz factors and angles to the line-of-sight can be calculated for the jet. For $\delta = 5$, $\Gamma$=7.5 and $\theta$=11°; for $\delta = 50$, $\Gamma$=25.5 and $\theta$=0.3°. Again, the equipartition brightness temperature limit implies values for 3C 279 near the extremes of expected EGRET source properties (Lister 1998). 3C 279 and NRAO 530 have both been detected by EGRET, and Bower & Backer (1998) speculate that blazars detected by EGRET may be those where the equipartition brightness temperature limit is briefly (on a timescale of years) superseded by the inverse Compton catastrophe limit. The observations presented in this paper occurred at the beginning of a total flux density flare at 5 GHz recorded by the Michigan monitoring program that would later reach the highest flux density yet recorded in this program for 3C 279 at 5 GHz. Measurements of the variability brightness temperature of this flare (Lähteenmäki, Valtaoja, & Wiik 1999) together with VSOP brightness temperatures measured during AO2 should allow calculation of the intrinsic brightness temperature and Doppler factor and allow us to estimate any departures from equipartition in this source.

## 5. CONCLUSIONS

We have presented the first space VLBI images of 3C 279, which are the highest resolution images yet obtained of this source at 5 and 1.6 GHz. The parsec-scale emission is dominated by the core and the jet component C4 which has been visible in VLBI images since 1985. The

1.6 GHz VSOP image and the 5 and 1.6 GHz VLBA-only images show emission from a jet extending to the southwest. The 1.6 GHz VLBA-only image has structure that matches that seen in the highest resolution VLA images, connecting the parsec and kiloparsec scale structures in this source.

We have exploited two of the main strengths of VSOP: the ability to obtain matched-resolution images to ground-based images at higher frequencies and the ability to measure high brightness temperatures. The spectral index map constructed from the 1.6 GHz VSOP image and the 5 GHz VLBA-only image has an unusually inverted spectral index in the core region, approaching the limiting value for synchrotron self-absorption of +2.5. An extensive error analysis conducted on the model-fit brightness temperatures reveals brightness temperature lower limits as high as $5 \times 10^{12}$ K. This lower limit is significantly above both the nominal inverse Compton and equipartition brightness temperature limits. The derived Doppler factor, Lorentz factor, and angle to the line-of-sight in the case of the equipartition limit are at the upper end of the range of expected values for EGRET blazars.

Part of the work described in this paper has been carried out at the Jet Propulsion Laboratory, California Institute of Technology, under contract with the National Aeronautics and Space Administration. A.E.W. acknowledges support from the NASA Long Term Space Astrophysics Program. We gratefully acknowledge the VSOP Project, which is led by the Japanese Institute of Space and Astronautical Science in cooperation with many organizations and radio telescopes around the world. The National Radio Astronomy Observatory is a facility of the National Science Foundation operated under cooperative agreement by Associated Universities, Inc. This research has made use of data from the University of Michigan Radio Astronomy Observatory which is supported by the National Science Foundation and by funds from the University of Michigan, and the NASA/IPAC extragalactic database (NED) which is operated by the Jet Propulsion Laboratory, California Institute of Technology, under contract with the National Aeronautics and Space Administration.

## REFERENCES

Abraham, Z. & Carrara, E.A. 1998, ApJ, 496, 172
Akujor, C.E., Lüdke, E., Browne, I.W.A., Leahy, J.P., Garrington, S.T., Jackson, N., & Thomasson, P. 1994, A&AS, 105, 247
Aller, H.D., Aller, M.F., Latimer, G.E., & Hodge, P.E. 1985, ApJS, 59, 513
Biretta, J.A., Moore, R.L., & Cohen, M.H. 1986, ApJ, 308, 93
Bower, G.C. & Backer, D.C. 1998, ApJ, 507, L117
Carrara, E.A., Abraham, Z., Unwin, S.C., & Zensus, J.A. 1993, A&A, 279, 83
Cohen, M.H., Cannon, W., Purcell, G.H., Shaffer, D.B., Broderick, J.J., Kellermann, K.I., & Jauncey, D.L. 1971, ApJ, 170, 207
Cotton, W.D., et al. 1979, ApJ, 229, L115
Cotton, W.D., et al. 1980, ApJ, 238, L123
de Pater, I. & Perley, R.A. 1983, ApJ, 273, 64
Edwards, P.G., Hirabayashi, H., Lovell, J.E.J., Piner,B.G., Unwin, S.C., & Wehrle, A.E. 1999, Astronomische Nachrichten, in press
Grandi, P., et al. 1996, ApJ, 459, 73
Hartman, R.C., et al. 1992, ApJ, 385, L1
Hartman, R.C., et al. 1996, ApJ, 461, 698
Hirabayashi, H., et al. 1999, Adv. Sp. Res., in press
Hirabayashi, H., et al. 1998, Science, 281, 1825
Kellermann, K.I. & Pauliny-Toth, I.I.K. 1969, ApJ, 155, L71
Kellermann, K.I., Vermeulen, R.C., Zensus, J.A. & Cohen, M.C. 1998, AJ, 115, 1295
Knight, C.A., et al. 1971, Science, 172, 52
Krichbaum, T.P., et al. 1997, A&A, 323, L17
Lähteenmäki, A., Valtaoja, E., & Wiik, K. 1999, ApJ, 511, 112
Leppänen, K.J., Zensus, J.A., & Diamond, P.J. 1995, AJ, 110, 2479
Linfield, R.P., et al. 1989, ApJ, 336, 1105
Linfield, R.P., et al. 1990, ApJ, 358, 350
Lister, M.L., & Marscher, A.P. 1997, ApJ, 476, 572
Lister, M.L., Marscher, A.P., & Gear, W.K. 1998, ApJ, 504, 702
Lister, M.L. 1998, Ph.D. thesis, Boston Univ.
Lovell, J.E.J. 2000, in The VSOP Symposium: High Energy Astrophysical Phenomena Revealed by Space-VLBI, in press
Maraschi, L., et al. 1994, ApJ, 435, L91
Moellenbrock, G.A., et al. 1996, AJ, 111, 2174
Pearson, T.J. 1995, in Very Long Baseline Interferometry and the VLBA, ed. J.A. Zensus, P.J. Diamond, & P.J. Napier (San Francisco:ASP), 267
Pilbratt, G., Booth, R.S., & Porcas, R.W. 1987, A&A, 173, 12
Rantakyrö, F.T., et al. 1998, A&AS, 131, 451
Readhead, A.C.S. 1994, ApJ, 426, 51
Shepherd, M.C., Pearson, T.J., & Taylor, G.B. 1994, BAAS, 26, 987
Shen, Z.Q., et al. 1999, PASJ, 51, 513
Tzioumis, A.K., et al. 1989, AJ, 98, 36
Unwin, S.C., Cohen, M.H., Biretta, J.A., Hodges, M.W., & Zensus, J.A. 1989, ApJ, 340, 117
Unwin, S.C., Wehrle, A.E., Lobanov, A.P., Zensus, J.A., Madejski, G.M., Aller, M.F., & Aller, H.D. 1997, ApJ, 480, 596
Unwin, S.C., Wehrle, A.E., Urry, C.M., Gilmore, D.M., Barton, E.J., Kjerulf, B.C., Zensus, J.A., & Rabaca, C.R. 1994, ApJ, 432, 103
Vermeulen, R.C. 1995, Proc. Natl. Acad. Sci., 92, 11385
Wardle, J.F.C., Homan, D.C., Ojha, R. & Roberts, D.H. 1998, Nature, 395, 457
Wehrle, A.E., et al. 1998, ApJ, 497, 178
Wehrle, A.E., Unwin, S.C., & Zook, A.C. 1994 in NRAO Workshop 23, Compact Extragalactic Radio Sources, ed. J.A. Zensus & K.I. Kellermann (Green Bank:NRAO), 197
Wehrle, A.E., Unwin, S.C., Zook, A.C., Urry, C.M., Marscher, A.P., & Teräsranta, H. 1996, in Blazar Continuum Variability, ed. H.R. Miller, J.R. Webb, & J.C. Noble (San Francisco:ASP), 430
Wehrle, A.E., et al. 2000, in preparation
Whitney, A.R., et al. 1971, Science, 173, 225